

Initiation and long-term instability of the East Antarctic Ice Sheet

Sean P. S. Gulick^{1*}, Amelia E. Shevenell^{2*}, Aleksandr Montelli^{1†}, Rodrigo Fernandez¹, Catherine Smith^{2‡}, Sophie Warny³, Steven M. Bohaty⁴, Charlotte Sjunneskog⁵, Amy Leventer⁶, Bruce Frederick^{1†} & Donald D. Blankenship¹

Antarctica's continental-scale ice sheets have evolved over the past 50 million years^{1–4}. However, the dearth of ice-proximal geological records^{5–8} limits our understanding of past East Antarctic Ice Sheet (EAIS) behaviour and thus our ability to evaluate its response to ongoing environmental change. The EAIS is marine-terminating and grounded below sea level within the Aurora subglacial basin, indicating that this catchment, which drains ice to the Sabrina Coast, may be sensitive to climate perturbations^{9–11}. Here we show, using marine geological and geophysical data from the continental shelf seaward of the Aurora subglacial basin, that marine-terminating glaciers existed at the Sabrina Coast by the early to middle Eocene epoch. This finding implies the existence of substantial ice volume in the Aurora subglacial basin before continental-scale ice sheets were established about 34 million years ago^{1–4}. Subsequently, ice advanced across and retreated from the Sabrina Coast continental shelf at least 11 times during the Oligocene and Miocene epochs. Tunnel valleys¹² associated with half of these glaciations indicate that a surface-meltwater-rich sub-polar glacial system existed under climate conditions similar to those anticipated with continued anthropogenic warming^{10,11}. Cooling since the late Miocene¹³ resulted in an expanded polar EAIS and a limited glacial response to Pliocene warmth in the Aurora subglacial basin catchment^{14–16}. Geological records from the Sabrina Coast shelf indicate that, in addition to ocean temperature, atmospheric temperature and surface-derived meltwater influenced East Antarctic ice mass balance under warmer-than-present climate conditions. Our results imply a dynamic EAIS response with continued anthropogenic warming and suggest that the EAIS contribution to future global sea-level projections^{10,11,15,17} may be under-estimated.

The EAIS response to anthropogenic warming and contribution to global sea level are the largest uncertainties in climate models because EAIS formation, evolution, and behaviour during past warm climates are poorly understood^{10,11}. Deep-sea benthic foraminifer oxygen isotopes ($\delta^{18}\text{O}$) indicate that during the early Eocene (53–51 million years ago; Myr ago), Earth experienced the warmest conditions^{1,4,17,18} of the past 65 Myr. This warmth was followed by about 15 Myr of cooling, declining atmospheric CO_2 , tectonic reorganizations, and the development of continental-scale Antarctic ice sheets by the earliest Oligocene (33.6 Myr ago)^{1–4,17–19}. As atmospheric CO_2 declined through the Oligocene and Miocene, deep-sea $\delta^{18}\text{O}$ and far-field (far from Antarctica) sea-level records suggest that ice sheets advanced to and retreated from Antarctica's continental shelves in response to astronomically paced changes in solar insolation^{3,4,18,20,21}. These records also suggest larger Antarctic ice sheets with less pronounced growth and decay cycles after the middle Miocene (about 13.8 Myr ago)^{1,4}, when global climate was cool and atmospheric CO_2 concentrations

low, relative to the Eocene and Oligocene^{4,17}. While far-field records provide a general framework for understanding Cenozoic Antarctic cryosphere development, these records provide little direct evidence for the ice location and extent or the thermal conditions required to assess the climate forcings and feedbacks involved in Antarctic cryosphere and global climate evolution; these records are also complicated by Northern Hemisphere ice volume in the Plio-Pleistocene epoch^{1,3,4}.

The East Antarctic continental margin and Southern Ocean sediments provide direct evidence of EAIS evolution, indicating that there existed regional marine-terminating ice in the late Eocene^{22–24} and astronomically paced glacial–interglacial cycles through the Pliocene^{5,6,14}. However, existing ice-proximal records are geographically limited and temporally discontinuous, making regional comparisons difficult. Recent ice-sheet models provide additional insight into EAIS evolution^{10,11,25}. Outputs indicate that EAIS catchments with deep landward-dipping subglacial topography and surface meltwater, including the Aurora subglacial basin (ASB), may be sensitive to climate perturbations (for example, atmospheric and/or oceanic temperatures, atmospheric CO_2 , sea level)^{9–11,25}. However, outputs depend on poorly constrained initial boundary conditions^{17,24,25}, feedbacks¹⁸, and retreat mechanisms¹¹. Thus, uncertainties remain regarding EAIS evolution that can only be resolved with well dated ice-proximal marine geological and geophysical data^{1,19}.

To improve predictions of future EAIS response to warming and contribution to global sea level rise^{10,11}, knowledge of EAIS evolution in catchments with large potential sea-level contributions is critical. The low-lying glacially sculpted ASB catchment (containing ice equivalent to a 3–5 m rise in sea level^{9,15,26}; Fig. 1a) drains ice from the Gamburtsev Mountains to the Sabrina Coast via the Totten Glacier, which is experiencing the largest mass loss in East Antarctica²⁷ and is influenced by warm subsurface (deeper than 400 m) ocean waters at its grounding line²⁸. The ASB catchment consists of several over-deepened basins^{15,26} and hosts an active subglacial hydrological system that drains basal meltwater to the ocean²⁹, suggesting that regional outlet glaciers may be susceptible to both progressive retreat¹³ and changing subglacial hydrology²⁹. Thus, regional glacial dynamics and, ultimately, sea-level contribution during a given warm interval depends on both catchment and glacier boundary conditions (for example, subglacial topography, substrate, and meltwater presence and volume) coupled to atmospheric and oceanic forcings.

We present the first ice-proximal marine geophysical and geological records of ASB glacial evolution (Methods; Figs 1b, 2, 3a). To document regional glacial development, ice dynamics, and the timing of major environmental transitions, we integrate seismic reflection and sedimentary data from the Sabrina Coast continental shelf, at the outlet of the ASB (Fig. 1b). This margin formed during Late Cretaceous period

¹Institute for Geophysics, Jackson School of Geosciences, University of Texas at Austin, Austin, Texas 78758, USA. ²College of Marine Science, University of South Florida, Saint Petersburg, Florida 33701, USA. ³Department of Geology and Geophysics and Museum of Natural Science, Louisiana State University, Baton Rouge, Louisiana 70803, USA. ⁴School of Ocean and Earth Science, University of Southampton, Southampton SO14 3ZH, UK. ⁵Antarctic Marine Geological Research Facility, Florida State University, Tallahassee, Florida 32306, USA. ⁶Geology Department, Colgate University, Hamilton, New York 13346, USA. [†]Present addresses: Scott Polar Research Institute, University of Cambridge, Cambridge CB2 1ER, UK (A.M.); International Ocean Discovery Program, Texas A&M University, 1000 Discovery Drive, College Station, Texas 77845, USA (C.S.); Department of Geology, University of Kansas, Lawrence, Kansas 66045, USA (B.F.).

*These authors contributed equally to this work.

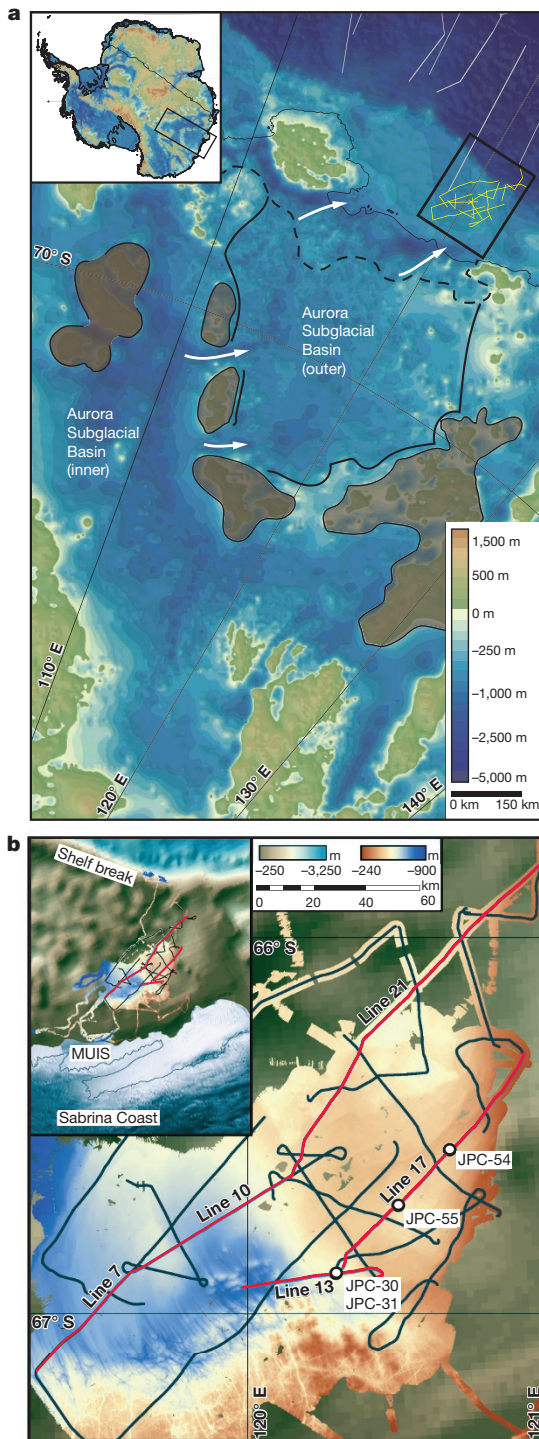


Figure 1 | ASB elevations and Sabrina Coast bathymetry. **a**, ASB elevations⁹ and Sabrina Coast shelf study location (black rectangle) with NBP14-02 (yellow) and published (white)³⁰ seismic lines indicated. The inset shows the ASB location (black rectangle) in Antarctica. ASB highlands (brown), reduced ice glacial pathways (white arrows)²⁶, approximate retreated Oligo–Miocene (solid line) and late Miocene–Pleistocene (dashed line) grounding-line locations¹⁵. **b**, NBP14-02 seismic lines (black), bathymetry and BEDMAP2 bathymetry⁹ with interpreted seismic lines (red) and jumbo piston cores (JPC; white) indicated. The inset shows regional bathymetry⁹ and seismics. The Sabrina Coast coastline (blue outline), Moscow University Ice Shelf (MUIS), and shelf break are indicated.

rifting of Antarctica and Australia, with tectonic subsidence continuing through the Palaeogene period⁸. The present-day continental shelf is about 200 km wide, about 600 m deep, and slopes landward (Fig. 1b).

We imaged around 1,300 m of dipping sedimentary strata that overlie acoustic basement on the inner continental shelf (Methods; Fig. 1b). We identified three distinct packages of sedimentary rocks bounded by basement, regionally extensive unconformities, and the sea floor, termed Megasequences I–III (MS-I, MS-II and MS-III; Figs 2a, c, 3a, Extended Data Fig. 1). Glacial erosion of the sea floor allowed us to recover and date strata near the top of MS-I and at the base of MS-III (Methods; Figs 2a, c).

The deepest unit, MS-I, overlies basement and consists of an approximately 620-m-thick, seaward-dipping sequence of low-amplitude discontinuous reflectors that increase in amplitude and lateral continuity upsection (Methods; Fig. 2a, Extended Data Fig. 1). No evidence of glacial erosion exists within these strata (Figs 2a and 3a, Extended Data Fig. 1). On the middle shelf, we imaged two intervals of inclined stratal surfaces (clinofolds), indicating times of high sediment flux to an unglaciated continental margin (Fig. 2a). The jumbo piston core NBP14-02 JPC-55 (1.69 m) recovered mica-rich silty sands 15–20 m below the upper clinofold (Methods; Fig. 2a, Extended Data Figs 1b, 2a, Extended Data Table 1). Terrestrial palynomorphs and benthic foraminifers indicate that these marine sediments are late Palaeocene in age (Methods; Fig. 2b, Extended Data Figs 1, 2, 5, Extended Data Tables 2, 3), confirming the pre-glacial seismic interpretation of MS-I.

Above the upper clinofold, within MS-I, are a series of moderate- to high-amplitude, laterally variable reflectors (grey shading; Methods; Fig. 2a, Extended Data Fig. 1). Piston core NBP14-02 JPC-54 (1.2 m; Methods; Fig. 2a, Extended Data Figs 1b, 3), recovered from this interval, contains centimetre-scale lonestones interpreted to be ice-rafted debris. Terrestrial palynomorphs indicate that these sediments are of early-to-middle Eocene age (Methods; Fig. 2b, Extended Data Table 2). Laterally variable reflectivity without chaotic seismic facies, with ice-rafted debris, and no evidence for cross-shelf glacial erosion indicate that marine-terminating glaciers were present at the Sabrina Coast by the middle Eocene, but grounded ice had not yet advanced across the shelf (Figs 2a, 3a).

MS-I strata reveal episodes of enhanced sediment flux from the ASB, followed by the early to middle Eocene arrival of marine-terminating glaciers to the Sabrina Coast. Models and observations indicate that Antarctica's ice sheets nucleated in the higher elevations of the Gamburtsev Mountains and first reached the ocean near the Sabrina Coast and Prydz Bay¹⁹, increasing sediment flux to the Australo-Antarctic Gulf³⁰. Within the ASB are a series of topographically constrained basins that probably hosted progressively larger ice volumes^{15,26} as ice expanded in the catchment (Fig. 1a). We speculate that after the early Eocene climate optimum (53–51 Myr ago), as regional and global temperatures cooled and atmospheric CO₂ declined^{17,18} (Fig. 3b, c), glacial ice breached the northern ASB highlands²⁶, allowing marine-terminating glaciers to deliver ice-rafted debris to the Sabrina Coast shelf by the early to middle Eocene (Figs 1a, 2a, Extended Data Fig. 2). This finding is important and indicates both the presence of substantial East Antarctic ice volume by the early to middle Eocene and the relatively early arrival of marine-terminating glaciers at the Sabrina Coast, compared with late Eocene arrivals in Prydz Bay and the Weddell Sea^{22–24}. Owing to the relative paucity of Eocene data from Antarctica's margins, it is not clear if this early arrival is unique to the Sabrina Coast, or if equivalent data have not yet been recovered.

Upsection (around 13 m) from core JPC-54, the deepest regionally mappable roughly eroded surface (dark-blue horizon; Figs 2a, 3a, Extended Data Fig. 1) separates MS-I strata from MS-II strata and provides the first preserved evidence of grounded ice on the Sabrina Coast shelf (Methods). MS-II is up to 675 m thick with ten additional erosive surfaces (grey numbered horizons; Fig. 3a, Extended Data Fig. 1) that truncate reflectors and exhibit rough morphology and channels indicative of glacial erosion in a meltwater-rich environment^{7,12,29,30} (Methods). Between erosive surfaces, we observe strata with parallel high-amplitude reflectivity and prograding strata of varying thickness

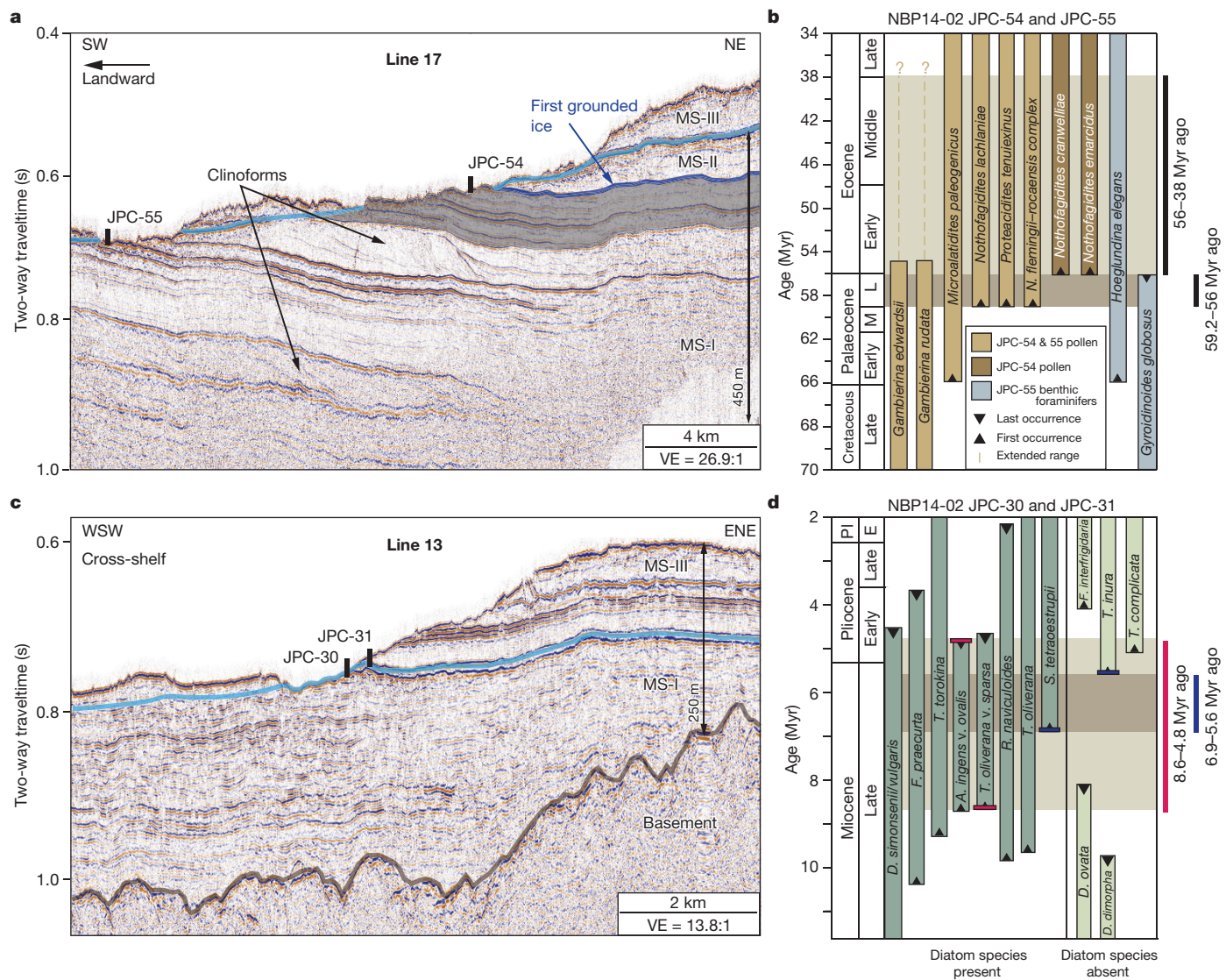


Figure 2 | Sabrina Coast seismic and piston core biostratigraphy. VE, vertical exaggeration. **a**, Seismic line 17 with core locations in MS-I (pre-glacial to pro-glacial; grey shading). MS-II (meltwater-rich glacial) overlies the first expression of grounded ice (dark-blue horizon). MS-III (polar glacial) overlies regional unconformity (light-blue horizon). **b**, Biostratigraphy for JPC-55, based on pollen and benthic foraminifers

(late Palaeocene; brown shading), and JPC-54, based on pollen (early to middle Eocene; beige shading). **c**, Seismic line 13 with core locations relative to regional unconformity (light-blue horizon). **d**, JPC-30 and JPC-31 diatom biostratigraphy, with conservative (beige shading, red line) and preferred (brown shading, blue line) ages.

(Methods), which indicate open marine conditions and intervals of high sediment flux^{7,8}, respectively, between the 11 glacial advances and retreats from the ASB.

Unlike previously imaged East Antarctic shelf sequences^{7,8}, Sabrina Coast MS-II reveals multiple erosive surfaces (2–6, 8 and 9) with U-shaped channels carved into sedimentary strata (Fig. 3a). Their geometry and size (Methods; ≤170 m deep; about 1,150 m wide) indicate that these channels are consistent with subglacial tunnel valleys observed in surface meltwater-rich sub-polar glacial systems¹². The most prominent channels are associated with surfaces 3–5, 8 and 9 (Fig. 3a, Extended Data Fig. 1e). Overlying erosive surface 11 (Fig. 3a, Extended Data Fig. 1e) is an approximately 330-m-thick sequence of seaward-dipping strata devoid of rough erosional surfaces, indicating prolonged continental shelf progradation and high sediment flux in an open marine setting^{7,8}. A regional landward-dipping angular unconformity truncates seaward-dipping MS-II (and in some places, MS-I) strata (light-blue horizon; Figs 2a, c, 3a, Extended Data Fig. 1). Late Miocene to earliest Pliocene diatomites were recovered from and immediately above the unconformity (Fig. 2c, d, Extended Data

Figs 1, 4, 6). Because we may not have recovered sediments below the unconformity, we consider the late Miocene (around 7–5.5 Myr ago) the youngest possible age for the MS-III base (Fig. 2d).

Ice advanced across the Sabrina Coast continental shelf at least 11 times from the early to middle Eocene to the late Miocene (Fig. 3a), when average atmospheric CO₂ concentrations (Fig. 3b), global temperatures (Fig. 3c), and global sea levels (Fig. 3d) were similar to or higher than at present^{4,17,18}. Without additional age constraints, the pacing of these glaciations is unknown, but far-field and ice-proximal records indicate cryosphere sensitivity to astronomically paced insolation changes during the Oligo–Miocene^{5,20,21}. The scale of the Sabrina Coast shelf tunnel valleys and the presence of similar channels within the ASB catchment, about 400 km from the present grounding line, suggest that regional subglacial hydrologic systems were fed by large volumes of surface meltwater during Oligo–Miocene glacial–interglacial cycles (Methods)^{11,15}. Thus, during climates similar to or warmer than present, surface-derived meltwater may play an important part in EAIS behaviour²⁹, as indicated by models¹¹. The prograding sequence at the top of MS-II is similar to middle to late

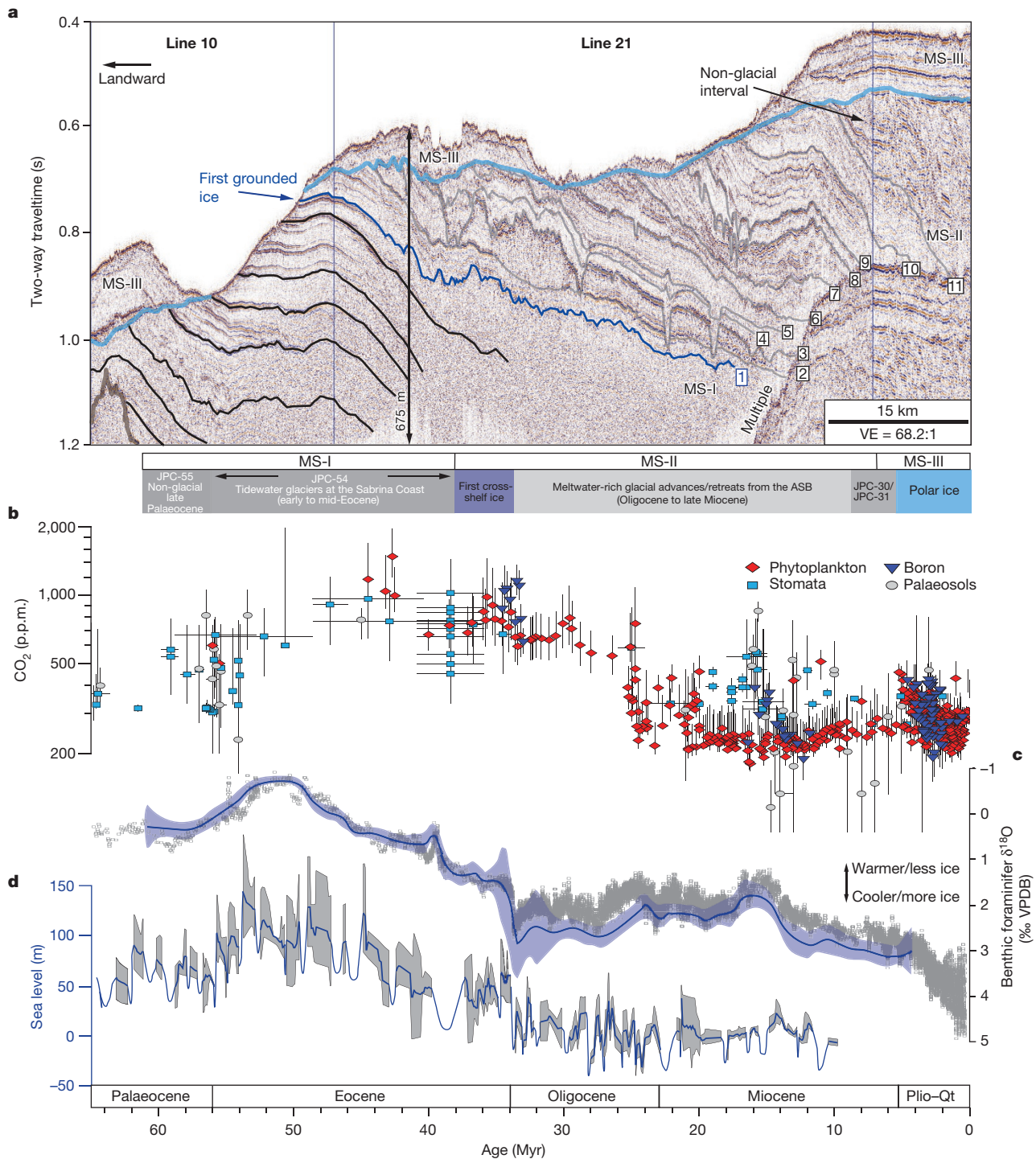


Figure 3 | Composite Sabrina Coast section with glacial surfaces and climate indicators. **a**, Composite seismic line with pre- to pro-glacial MS-I (black), glacial MS-II with erosion surfaces (first dark-blue, then grey) overlaid by a non-glacial interval and regional unconformity (light-blue), and polar glacial MS-III. **b**, Cenozoic atmospheric CO_2 reconstructions^{17,18} with two-standard-deviation error bars (black).

Miocene sequences in Wilkes Land and Prydz Bay, which reflect the transition from sub-polar to polar glacial regimes^{7,8} (Fig. 3a, Extended Data Fig. 1e).

Above the regional unconformity, MS-III consists of a 0–110-m-thick veneer of sub-horizontal to landward-dipping strata that thicken landward, indicating substantial glacial erosion of MS-II or lower regional sediment flux and onset of ice loading by the late Miocene⁸ (Methods; Figs 2a, c, 3a, Extended Data Fig. 1). MS-III strata contain no visible

c, Composite high-latitude benthic foraminifer $\delta^{18}\text{O}$ record with blue uncertainty band generated/calculated as in ref. 4, reflecting global ice volume and deep ocean temperatures⁴; VPDB, Vienna Pee-Dee belemnite standard. **d**, New Jersey margin sea-level reconstructions (black) with minimum uncertainty (grey envelope) and best estimates (blue line)³.

channels, suggesting reduced regional surface meltwater influence and more diffuse basal meltwater flux^{12,15,26,29}. High-amplitude reflectors (Fig. 3a) within acoustically chaotic MS-III strata indicate erosional surfaces in late Miocene to Pleistocene tills (Methods) and advance or retreat of an expanded EAIS¹⁵. Open marine sediments are present, but the lack of accumulation and preservation suggests limited regional ice retreat or shorter interglacials since the late Miocene (Methods; Figs 2c and 3a, Extended Data Fig. 1).

An expanded polar EAIS occupied the ASB catchment and the Sabrina Coast continental shelf since the late Miocene¹⁵, coincident with global climate, carbon and hydrologic cycle reorganizations^{4,13}, continent-wide ice-sheet expansion and stabilization^{7,8,13}, Antarctic Circumpolar Current intensification, Southern Ocean cooling, and modern meridional thermal gradient development (Fig. 3b)^{1,13}. Atmospheric cooling probably limited the amount of regional surface ablation, resulting in ice expansion and reduced surface-derived meltwater in the ASB catchment. Although open marine conditions intermittently existed on the shelf, the relative MS-III thickness and patterns of erosion within the ASB catchment suggest a maximum grounding-line retreat¹⁵ of about 150 km from its present location since the late Miocene. Thus, in contrast to the adjacent Wilkes subglacial basin¹⁴, the ASB did not contribute substantially to sea level rise during Pliocene warmth^{15,16}.

Sabrina Coast shelf records reveal the importance of atmospheric temperatures and surface-derived meltwater to Antarctica's ice mass balance. Although deeper, more continuous sampling of these sediments is required to assess the timing, magnitude and rates of EAIS evolution in the ASB, the ice-proximal Sabrina Coast shelf record confirms model predictions of the region's long-term sensitivity to climate^{10,11,15,25,26}. Critical for future global sea-level rise scenarios is the potential for ASB catchment glaciers to revert from the extensive polar system of the past 7 Myr to the surface meltwater-rich sub-polar system of the Oligo-Miocene (Fig. 3a), when average global temperatures and atmospheric CO₂ concentrations were similar to those anticipated under current warming projections (Fig. 3b, c)^{10,11,17}. At present, the Totten Glacier is thinning faster than any other East Antarctic outlet glacier^{11,27,28} owing to ocean thermal forcing²⁸. Our findings suggest that ice in the ASB catchment may respond dramatically to anthropogenic climate forcing if regional atmospheric warming results in surface meltwater production.

Online Content Methods, along with any additional Extended Data display items and Source Data, are available in the online version of the paper; references unique to these sections appear only in the online paper.

Received 16 May; accepted 6 November 2017.

- Kennett, J. P. Cenozoic evolution of Antarctic glaciation, the circum-Antarctic ocean, and their impact on global paleoceanography. *J. Geophys. Res.* **82**, 3843–3860 (1977).
- Coxall, H. K. *et al.* Rapid stepwise onset of Antarctic glaciation and deeper calcite compensation in the Pacific Ocean. *Nature* **433**, 53–57 (2005).
- Kominz, M. A. *et al.* Late Cretaceous to Miocene sea-level estimates from the New Jersey and Delaware coastal plain coreholes: an error analysis. *Basin Res.* **20**, 211–226 (2008).
- Mudelsee, M., Bickert, T., Lear, C. H. & Lohmann, G. Cenozoic climate changes: a review based on time series analysis of marine benthic $\delta^{18}\text{O}$ records. *Rev. Geophys.* **52**, 333–374 (2014).
- Naish, T. R. *et al.* Orbitally induced oscillations in the East Antarctic ice sheet at the Oligocene/Miocene boundary. *Nature* **413**, 719–723 (2001).
- Naish, T. R. *et al.* Obliquity-paced Pliocene West Antarctic ice sheet oscillations. *Nature* **458**, 322–328 (2009).
- Cooper, A. K. *et al.* in *Antarctic Climate Evolution. Developments in Earth and Environmental Sciences* (eds Florindo, F. & Siebert, M.) 115–228 (Elsevier, 2009).
- Escutia, C., Brinkhuis, H., Klaus, A. & Expedition 318 Scientists. Wilkes Land Glacial History. *Proc. Integrated Ocean Drilling Program* **318**, <http://doi.org/10.2204/iodp.proc.318.2011> (Ocean Drilling Program Management International, 2011).
- Fretwell, P. *et al.* Bedmap2: improved ice bed, surface and thickness datasets for Antarctica. *Cryosphere* **7**, 375–393 (2013).
- Golledge, N. R. *et al.* The multi-millennial Antarctic commitment to future sea-level rise. *Nature* **526**, 421–425 (2015).

- DeConto, R. M. & Pollard, D. Contribution of Antarctica to past and future sea-level rise. *Nature* **531**, 591–597 (2016).
- Kehew, A. E., Piotrowski, J. A. & Jørgensen, F. Tunnel valleys: concepts and controversies. *Earth Sci. Rev.* **113**, 33–58 (2012).
- Herbert, T. D. *et al.* Late Miocene global cooling and the rise of modern ecosystems. *Nat. Geosci.* **9**, 843–847 (2016).
- Cook, C. P. *et al.* Dynamic behavior of the East Antarctic ice sheet during Pliocene warmth. *Nat. Geosci.* **6**, 765–769 (2013).
- Aitken, A. R. A. *et al.* Repeated large-scale retreat and advance of Totten Glacier indicated by inland bed erosion. *Nature* **533**, 385–389 (2016).
- Rovere, A. *et al.* The Mid-Pliocene sea-level conundrum: glacial isostasy, eustasy, and dynamic topography. *Earth Planet. Sci. Lett.* **387**, 27–33 (2014).
- Masson-Delmotte, V. *et al.* in *Climate Change 2013: The Physical Science Basis. Contribution of Working Group I to the Fifth Assessment Report of the Intergovernmental Panel on Climate Change* (eds Stocker, T. F. *et al.*) 383–464 (Cambridge Univ. Press, 2013).
- Anagnostou, E. *et al.* Changing atmospheric CO₂ concentration was the primary driver of early Cenozoic climate. *Nature* **533**, 380–384 (2016).
- DeConto, R. M. & Pollard, D. Rapid Cenozoic glaciation of Antarctica induced by declining atmospheric CO₂. *Nature* **421**, 245–249 (2003).
- Pälike, H. *et al.* The heartbeat of the Oligocene climate system. *Science* **314**, 1894–1898 (2006).
- Liebrand, D. *et al.* Evolution of the early Antarctic ice ages. *Proc. Natl Acad. Sci. USA* **114**, 3867–3872 (2017).
- Scher, H. D., Bohaty, S. M., Smith, B. W. & Munn, G. H. Isotopic interrogation of a suspected late Eocene glaciation. *Paleoceanography* **29**, 628–644 (2014).
- Carter, A., Riley, T. R., Hillenbrand, C.-D. & Rittner, M. Widespread Antarctic glaciation during the late Eocene. *Earth Planet. Sci. Lett.* **458**, 49–57 (2017).
- Passchier, S., Ciarletta, D. J., Miriagos, T. E., Bijl, P. K. & Bohaty, S. M. An Antarctic stratigraphic record of stepwise ice growth through the Eocene-Oligocene transition. *GSA Bull.* **129**, 318–330 (2017).
- Golledge, N. R., Levy, R. H., McKay, R. M. & Naish, T. R. East Antarctic ice sheet most vulnerable to Weddell Sea warming. *Geophys. Res. Lett.* **44**, 2343–2351 (2017).
- Young, D. A. *et al.* A dynamic early East Antarctic Ice Sheet suggested by ice-covered fjord landscapes. *Nature* **474**, 72–75 (2011).
- Li, X., Rignot, E., Mougnot, J. & Scheuchl, B. Ice flow dynamics and mass loss of Totten Glacier, East Antarctica, from 1989 to 2015. *Geophys. Res. Lett.* **43**, 6366–6373 (2016).
- Rintoul, S. R. *et al.* Ocean heat drives rapid basal melt of the Totten Ice Shelf. *Sci. Adv.* **2**, e1601610 (2016).
- Wright, A. P. *et al.* Evidence of a hydrological connection between the ice divide and ice sheet margin in the Aurora Subglacial Basin, East Antarctica. *J. Geophys. Res.* **117**, F01033 (2012).
- Close, D. I., Stagg, H. M. J. & O'Brien, P. E. Seismic stratigraphy and sediment distribution on the Wilkes Land and Terre Adélie margins, East Antarctica. *Mar. Geol.* **239**, 33–57 (2007).

Supplementary Information is available in the online version of the paper.

Acknowledgements We thank the NBP14-02 science party, the ECO captain and crew, and the ASC technical staff aboard the RV/IB *N. B. Palmer*. NBP14-02 was supported by the National Science Foundation (grants NSF PLR-1143836, PLR-1143837, PLR-1143843, PLR-1430550 and PLR-1048343) and a GSA graduate student research grant (to C.S.). We thank the Antarctic Marine Geology Research Facility staff at Florida State University for sampling assistance and E. Thomas, M. Katz, F. Sangiorni, P. Bijl and S. Manchester for discussions. This is UTIG Contribution #3137.

Author Contributions S.P.S.G. and A.E.S. contributed equally to this work, co-writing the manuscript with input from all authors. D.D.B., S.P.S.G., A.L. and A.E.S. conceived the study. B.F., R.F., S.P.S.G., A.L., A.E.S., C.S. and the shipboard scientific party collected geophysical data and samples on USAP cruise NBP14-02. All authors contributed to the analyses and interpretation of the results.

Author Information Reprints and permissions information is available at www.nature.com/reprints. The authors declare no competing financial interests. Readers are welcome to comment on the online version of the paper. Publisher's note: Springer Nature remains neutral with regard to jurisdictional claims in published maps and institutional affiliations. Correspondence and requests for materials should be addressed to S.G. (sean@ig.utexas.edu).

Reviewer Information *Nature* thanks K. Billups, A. Bruch, S. Greenwood and the other anonymous reviewer(s) for their contribution to the peer review of this work.

METHODS

Seismic data acquisition, processing and interpretation. The 750 km of 3-m resolution multichannel seismic data were acquired using dual 45-cubic-inch generator–injector guns and a 75-m-long, 24-channel streamer in 2014 in heavy ice conditions aboard the *R/V/B N. B. Palmer*. Data processing followed standard steps of filtering, spherical divergence correction, normal moveout correction, and muting, but no deconvolution was required, because of the quality of the generator–injector source. All sediment thicknesses are presented in meters and based on a velocity of $2,250 \text{ m s}^{-1}$; seafloor depths are based on a velocity of $1,500 \text{ m s}^{-1}$. The acoustic basement is the limit of our reflectivity and interpreted as crystalline rock.

Seismic megasequences were identified on the basis of the presence or absence of erosional surfaces and seismic facies of the mappable units within the sediment packages. Seismic facies observed include: (1) stratified (laminated) or semi-stratified intervals interpreted as open marine, (2) relatively continuous layers with variable reflectivity interpreted as open marine conditions influenced by ice-rafting, and (3) chaotic, discontinuous or transparent intervals interpreted as glacial to periglacial conditions. MS-I exhibits stratified, semi-stratified and variably reflective (grey shading) intervals. MS-II exhibits chaotic and discontinuous intervals related to erosive surfaces, stratified or semi-stratified intervals, and prograding intervals. Rough, undulatory surfaces are indicators of glacial advance on continental shelves³¹. MS-III consists of chaotic or acoustically transparent intervals with thin intervals of stratified facies. The thickness of stratified intervals between erosional surfaces may be a proxy for duration of open water conditions and extent of ice retreat (and thus time and distance required for readvance)³². Therefore, MS-II includes extensive and long-lasting glacial retreats, whereas MS-III records localized or relatively short-lived retreats.

All identified horizons are regionally mappable within the seismic survey area. Glacial erosion surfaces are interpreted based on roughness, extent of down-cutting, and association with overlying chaotic or discontinuous facies. Tunnel valley determinations are based on comparisons with imaged tunnel valleys from the North Sea, Alaska, and Svalbard^{32–38}. Hydrologic modelling suggests that tunnel valleys form only when meltwater exceeds the capacity of flow through porous glacial substrate and any sheet flow at the base of a glacier³⁹. Because tunnel valley size is expected to relate to discharge of subglacial meltwater, the Sabrina Coast glacial erosion surfaces 3–5, 8 and 9 are interpreted as meltwater-rich glaciations that probably required surface-derived meltwater. In the Ross Sea, a widespread regional unconformity that separates prograding shelf strata from glacial tills was interpreted to indicate widespread ice-sheet expansion and the onset of ice loading, as suggested for the Sabrina Coast angular unconformity underlying MS-III⁴⁰. Uninterpreted versions of the seismic profiles in Figs 2a, c, and 3a, including individual lines from the regionally representative cross-shelf composite line (Fig. 3a), are included in Extended Data Fig. 1.

Marine sediment collection and physical properties. Marine sediments were collected in 440–550 m of water 100–150 km offshore, on the Sabrina Coast continental shelf (Extended Data Table 1). Geophysical data guided the recovery of a suite of four <2-m-long piston cores that targeted outcropping reflectors on the continental shelf (Figs 1b, 2a, c, Extended Data Figs 2–4). Seismic data, lithology, benthic foraminifers, diatoms, and bulk sediment geochemistry confirm that these sequences were deposited in open marine to subglacial settings. Sediment cores were transported (unsplit and at 4°C) to the Antarctic Marine Geological Research Facility at Florida State University, where they were split, photographed, visually described, X-rayed, and the GEOTEK Multi-sensor Core Logger instrument's data were collected following standard protocols. The radiographs were interpreted in Adobe Photoshop with the contrast adjusted for each image. Organic carbon, $\delta^{13}\text{C}$ and $\delta^{15}\text{N}$ analyses of bulk sediments were conducted using a Carlo Erba 2500 Elemental Analyzer coupled to a continuous flow ThermoFinnigan Delta Plus XL IRMS at the College of Marine Science, University of South Florida, following standard methods. Lithologic, physical properties, and geochemical data are shown in Extended Data Figs 2–4 and provided in Supplementary Information.

Core JPC-55 (1.69 m) contains two distinct lithologic units (Extended Data Fig. 2b). The upper unit (0–0.4 m; Unit 1) consists of Quaternary-recent diatom-rich sandy silt with relatively high magnetic susceptibility (Supplementary Information) overlying a more consolidated lower unit (0.4–1.69 m; Unit 2) of homogeneous black micaceous silty fine sands with organic detritus, rare pyrite nodules, macro- and microfossils, and an approximately 10-cm-diameter spherical siderite concretion nucleated around a monocot stem (Extended Data Fig. 2b, d and e; Supplementary Information).

Core JPC-54 (1.21 m), collected above the youngest clinof orm, contains two distinct lithologic units (Fig. 2a, Extended Data Fig. 3b). The lithology of the upper unit (0–0.2 m; Unit 1) in JPC-54 is similar to that of JPC-55 and overlies a lower unit (0.2–1.21 m; Unit 2) composed of structureless gravel-rich sandy silts to silty coarse sands with centimetre-scale angular limestones throughout Units 1 and 2 (Extended Data Fig. 3b). A conservative approach to interpretation of ice-

rafted debris was undertaken in these sediments so that only angular limestones exceeding 1 cm were interpreted to be ice-rafted debris. Lighter-coloured sediment with modern diatoms, visible on the right-hand side of JPC-54, indicates flow-in below approximately 0.8 m, probably due to a partial piston stroke; flow of dark sediment along the right side of the upper core is consistent with this interpretation and on-deck or transport disturbance (Extended Data Fig. 3b). However, angular limestones are observed throughout and a majority are surrounded by the dark-coloured sediments.

Core JPC-30 (0.52 m plus cutter nose) contains diatom-bearing sandy muds, with intervals of well sorted sands (0–0.25 m). Sub-angular diatomite clasts are present in a mud matrix between 0.25 m and 0.52 m. In the core cutter nose, we recovered stratified diatomite and gravelly diatom-bearing sandstone and sandy diatomite above a sharp contact with sandy diamictite below (Extended Data Fig. 4b).

Core JPC-31 (0.47 m) contains an upper unit of muddy diamicton (0–0.29 m). Between 0.29 m and 0.47 m, angular diatomite clasts are present, which may have been fractured during coring (Extended Data Fig. 4c).

Biostratigraphic methods. Palynology. Nine samples from JPC-54 and eight samples from JPC-55 (Extended Data Figs 2b, 3b, Extended Data Table 2) were processed at Global Geolab Limited, Alberta, Canada, using palynological techniques suited for Antarctic sediments. Approximately 5 g of dried sediment were weighed and spiked with a known quantity of *Lycopodium* spores to allow computation of palynomorph concentrations. Acid-soluble minerals (carbonates and silicates) were removed via digestion in the acids HCl and HF. Residues were concentrated by filtration through a $10\text{-}\mu\text{m}$ sieve and mounted on microscope slides for analyses. Analysis was conducted under $100\times$ oil immersion objective with a Zeiss Axio microscope. For samples with sufficient palynomorph abundance, a minimum of 300 palynomorphs were tabulated per sample. For samples with low abundance, the entire residue was tabulated. A database of all palynomorphs recovered was prepared and key species were photographically documented. The taxonomic evaluation was completed based on the type specimen repository and library at the Louisiana State University Center for Excellence in Palynology (CENEX). Palynological results are presented in Extended Data Table 2.

Benthic foraminifera. Benthic foraminifer counts and biostratigraphic data were generated for 16 depths in JPC-55 and 5 depths in JPC-54 using standard protocols (Extended Data Figs 2b, 5, Extended Data Table 3). Sediment samples between 20 cm^3 and 30 cm^3 were washed over a $63\text{-}\mu\text{m}$ sieve with deionized water. Sample residues were dried at 50°C for 24 h, transferred to labelled vials, dry-sieved into $250\text{-}\mu\text{m}$ and $150\text{-}\mu\text{m}$ fractions, and examined using a Zeiss Stemi 2000-C stereomicroscope with a $1.6\times$ lens and $10\times$ eyepiece (magnification $10.4\text{--}80\times$). Genus and species identifications were refined using a scanning electron microscope (SEM) at the University of South Florida College of Marine Science (Extended Data Fig. 5). All benthic foraminifer individuals present in each JPC-55 sample are tabulated in Extended Data Table 3. In JPC-55, preservation of aragonite and calcium carbonate tests, determined both visually and via SEM, ranges from poor to excellent (Extended Data Fig. 5). Five species of well-preserved aragonitic and calcareous benthic foraminifers were observed throughout JPC-55 Unit 2 (Extended Data Table 3). No foraminifers were observed in JPC-54.

Diatoms. Diatom biostratigraphy was conducted on two sets of NBP14-02 samples: (1) JPC-30 cutter nose diatomites and (2) diatomite clasts from the bottom of JPC-31 (Extended Data Figs 4b, d, 6). Quantitative slides were prepared at Colgate University for diatom assemblage studies and biostratigraphic evaluation using a settling technique that results in a random and even distribution of frustules⁴¹; sub-samples were sieved at $10\text{-}\mu\text{m}$ and $63\text{-}\mu\text{m}$ to concentrate unbroken frustules for examination. Photographic documentation at $1,000\times$ magnification using oil immersion on Olympus BX50 and BX60 microscopes was completed at Colgate University (Extended Data Fig. 6). The beige shading in Fig. 2d represents the conservative zonal assignment and age range, whereas the brown shading represents the refined age interpretation. Age constraints for key diatom bioevents are derived from the statistical compilation and analysis of average age ranges for Southern Ocean taxa⁴².

Chronology. Palynological biostratigraphic zonation scheme. Palynological biostratigraphic zonation of cores NBP14-02 JPC-54 and JPC-55 is based on the presence of a few key species and limited data available from Antarctica and surrounding regions (for example, Australia and New Zealand). *Gambierina edwardsii* and *Gambierina rudata* are known as Cretaceous to Palaeocene species. A recent study published a robust last appearance date (LAD) for these species at the Palaeocene/Eocene boundary on the East Tasman Rise (ODP Site 1172)⁴³. However, in southeastern Australia, the two *Gambierina* species observed in the Sabrina Coast sequence range into the earliest early Eocene⁴⁴. Extended ranges for the *Gambierina* sp. (dashed lines; Fig. 2b) are based on the palynological analysis of ODP Site 1166 in Prydz Bay^{45,46}, where abundant well preserved *Gambierina* specimens were observed and not considered reworked. Consequently,

the *Gambierina* sp. range was extended into the early to mid-Eocene in East Antarctica^{45,46}.

Microalattidites paleogenicus has a Palaeogene to Neogene range⁴⁶. Although we are adopting their range herein, there is some controversy with this range. The first occurrence of *Microalattidites paleogenicus* is listed as Senonian in Australia and New Zealand⁴⁷, but there is no robust evidence supporting an extended range in Antarctica. In the Fossilworks database (PaleoDB taxon number 321781 at <http://fossilworks.org/>), *Microalattidites paleogenicus* is listed in the range 55.8–11.608 Myr ago.

Nothofagidites lachlaniae ranges from the Palaeogene to modern times while *Nothofagidites flemingii-rocaensis* ranges from the Palaeogene to the Neogene⁴⁶. The range for *N. lachlaniae* in New Zealand is listed as Late Cretaceous to present and is similar to other forms⁴⁸. In the Palaeocene and Eocene, there is climatically induced variability observed in the *Nothofagidites* ranges. For example, broad regional vegetation changes (for example, the abundance of *Nothofagidites lachlaniae* in western Southland (the Ohai, Waiau and Balleny basins) and its scarcity in other Eocene sections (Waikato, the Taranaki basin, and the west coast of New Zealand's South Island) may be related to palaeoenvironmental factors⁴⁹. The type material is Pliocene⁵⁰, but the distinction of this species from other *Fuscospora* pollen (including *N. brachyspinulosa* and *N. waipawaensis*) is problematic. If *N. waipawaensis* and *N. senectus* are excluded, then the New Zealand first appearance date (FAD) of other *Fuscospora* pollen would be late Palaeocene.

In Southern Australia, the FAD of *N. flemingii* is in the upper part of the *Lygistepollenites balmei* Zone (late Palaeocene)^{51,52}. However, in a detailed study of Palaeocene–Eocene transition strata in western Victoria, *N. flemingii* is not reported⁵³. In New Zealand, the *N. flemingii* FAD is reported as middle Eocene^{54,55}. However, in well dated early Eocene New Zealand localities, occasional small *N. flemingii*-like specimens are observed; their identification is under debate. Owing to the relative geographic proximity of East Antarctica and Southern Australia in the Palaeogene, we follow refs 52 and 53 and place the FADs of both species in the late Palaeocene.

Proteacidites tenuixinus has a range from 66.043 Myr ago to 15.97 Myr ago (PaleoDB taxon number 277519 at <http://fossilworks.org/>). We adopt the published late Palaeocene *Proteacidites tenuixinus* FAD in southeastern Australia⁵¹, but acknowledge that the FAD could be as early as the early Palaeocene.

Two pollen species present in core JPC-54 were not observed in core JPC-55, *Nothofagidites cranwelliae* and *Nothofagidites emarcidus*. Most verified references for *Nothofagidites cranwelliae* and *Nothofagidites emarcidus* (for example, those with specimens properly identified; the *Nothofagidites* group is diverse, complex and easily misidentified) place the FAD of both of these species in the early Eocene, at the earliest^{56,57}. The latter species was also found in the Eocene of Western Australia⁵⁸.

Diatom preservation and biostratigraphy. The diatom assemblages present in cores JPC-30 and JPC-31 are indistinguishable, although preservation is better and abundance higher in the JPC-31 diatomites compared to the sandy diatom muds recovered in JPC-30. Overall, preservation is moderate to good in JPC-31 and poor to moderate in JPC-30 (Extended Data Fig. 6). Diatoms in both cores suffer from a high degree of fragmentation. Large centric taxa, such as *Actinocyclus* spp. and *Thalassiosira* spp., are generally broken, whereas the smaller centric and pennate specimens are well preserved (Extended Data Fig. 6). *Denticulopsis* specimens are generally well preserved, although the longer specimens of *D. delicata* are typically broken. *Rouxia* spp. occur mostly in fragments, making identification more problematic. Similarly, specimens of *Fragilariopsis* spp. are mostly present as broken specimens, with the exception of a few *F. praecurta* specimens (Extended Data Fig. 6).

Many of the diatom species present in both JPC-30 and JPC-31 have long age ranges and do not provide good biostratigraphic age constraints (for example, *Coccinodiscus marginatus*, *Trinacria excavata*). However, the presence of several common taxa provides robust support for a late Miocene–earliest Pliocene age. These taxa include: *Actinocyclus ingens* var. *ovalis*, *Denticulopsis delicata*, *Fragilariopsis praecurta*, *Thalassiosira oliverana* var. *sparsa*, *Thalassiosira torokina* (large form), and silicoflagellates in the *Distephanus speculum speculum* 'pseudofibula plexus' group. There is very little evidence of reworking of older material, with only one specimen of *Pyxilla* sp. and a fragment of *Hemiaulus* sp. observed; all species within both of these genera are typical of the Eocene and Oligocene.

Age determination for JPC-55 sediments. On the basis of our conservative pollen zonation scheme, we favour a late Palaeocene to earliest early Eocene age for the exceptionally diverse JPC-55 *in situ* fossil pollen assemblage; this assemblage is easily distinguishable from reworked Cretaceous microfossils present in the sediments (Fig. 2b). The presence of middle bathyal benthic foraminifer species *Gyroidinoides globosus* and *Palmula* sp., both of which went extinct at the Palaeocene–Eocene boundary⁵⁹, enables us to refine the pollen-based age

designation further to the late Palaeocene (Extended Data Fig. 5). Although its first occurrence may be diachronous, the presence of aragonitic Cenozoic benthic foraminifer species *Hoeglundina elegans*^{59–63} indicates that these sediments are Cenozoic in age, confirming the interpretation that co-occurring Cretaceous microfossils are reworked. *H. elegans* and other aragonitic benthic foraminifers are most common in upper to middle bathyal assemblages along the southern Australian margin and the Australo–Antarctic Gulf during the Palaeocene and Eocene^{60,63}. Thus, we conservatively designate an age of late Palaeocene to sediments in the lower unit (Unit 2) of JPC-55 (Fig. 2b, Extended Data Fig. 2b).

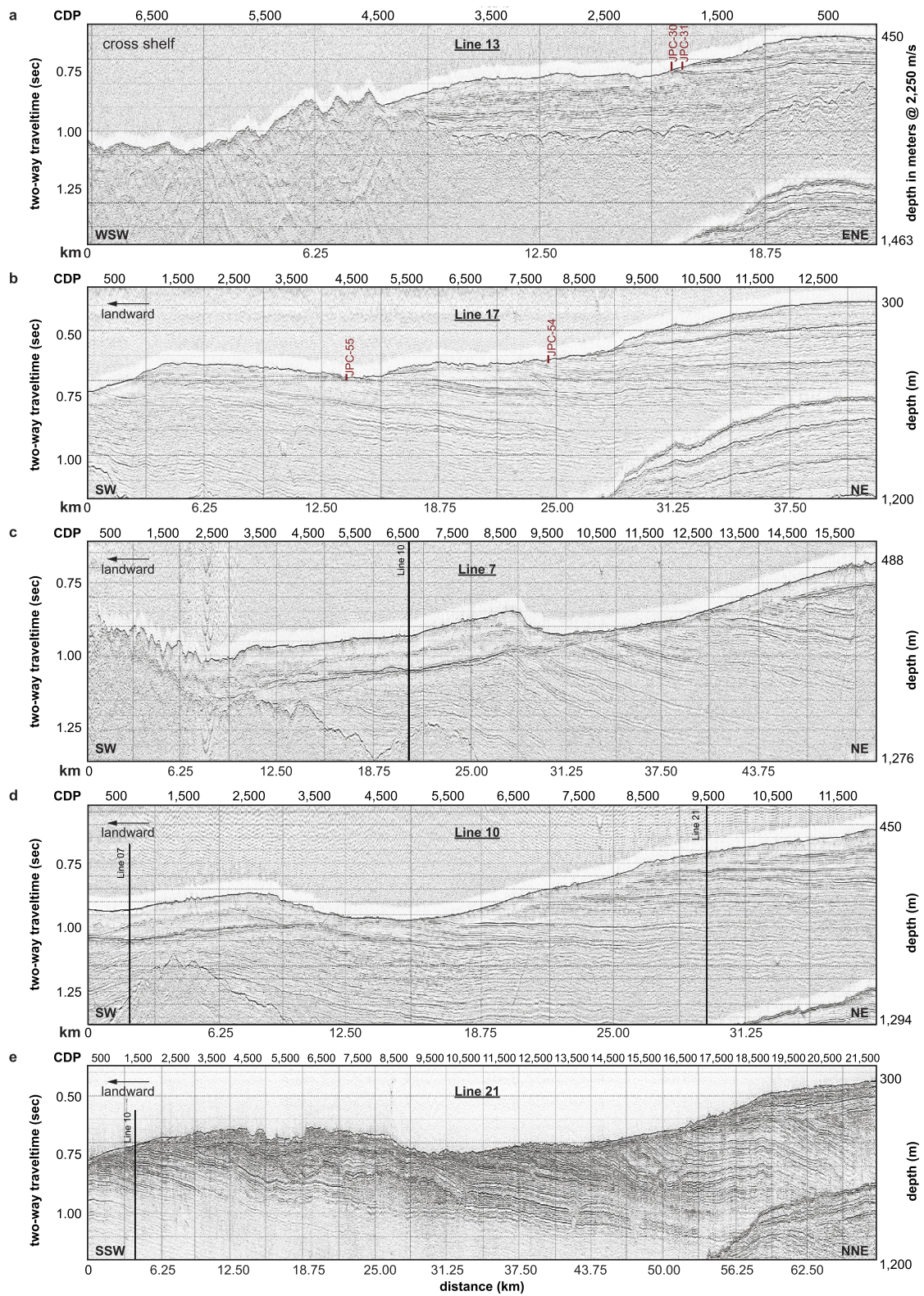
Age determination for JPC-54 sediments. Pollen biostratigraphy constrains the depositional age of JPC-54 Unit 2 sediments to the early to mid-Eocene (Fig. 2b, Extended Data Fig. 3b). No foraminifers are observed in the lower lithologic unit of JPC-54. Thus, based on the pollen assemblage alone, we favour an early to middle Eocene age for sediments in the lower unit (Unit 2) of JPC-54.

Age determination for JPC-30 and JPC-31 sediments. Based on Southern Ocean diatom ages⁴², the FAD of *T. oliverana* var. *sparsa* (8.61 Myr) and the LAD of *T. ingens* var. *ovalis* (4.78 Myr) provide a conservative age estimate for the diatom assemblages present in JPC-30 and JPC-31 (8.61–4.78 Myr; Fig. 2d). A more restricted age interpretation is possible if the presence of *Shionodiscus tetraoestrupii* (FAD 6.91 Myr) and the absence of the typical early Pliocene taxon *Thalassiosira inura* (FAD 5.59 Myr) are considered, indicating an age of 6.91–5.59 Myr (Fig. 2d). This more restricted age should be considered tentative, since precise calibrations for many Southern Ocean diatom bioevents in the Chron C3–C3A (4.2–7.1 Myr ago) interval are compromised by multiple short hiatuses at many drill sites and poor magnetostratigraphy. Further age refinement for the JPC-30 and JPC-31 samples will become possible as diatom biostratigraphic data are published for expanded late Neogene sections recovered on the Wilkes Land margin⁶⁴. However, the more conservative age estimate (8.61–4.78 Myr ago; Fig. 2d) is well supported by the presence of several taxa with well calibrated ages in the Southern Ocean, including *Rouxia naviculoides* (FAD 9.84 Myr ago), *Thalassiosira oliverana* (FAD 9.73 Myr ago), and *Thalassiosira torokina* (FAD 9.36 Myr ago). The absence of *Denticulopsis dimorpha* (LAD 9.75 Myr ago), *Denticulopsis ovata* (LAD 8.13), *Thalassiosira complicata* (FAD 5.12 Myr ago), *Fragilariopsis barronii* (FAD 4.38 Myr ago), and *Fragilariopsis interfrigidaria* (FAD 4.13 Myr ago) support this age assessment.

Data availability. The seismic data from the study are available in the Academic Seismic Datacentre at the University of Texas Institute for Geophysics (<http://www-udc.ig.utexas.edu/sdc/cruise.php?cruiseIn=nbp1402>). Sediment cores are archived in the NSF-funded Antarctic Core Repository at Oregon State University. All other data that support the findings of this study are available within the paper and its Supplementary Information; these data may also be downloaded from the US Antarctic Program Data Center (<http://www.usap-dc.org/>).

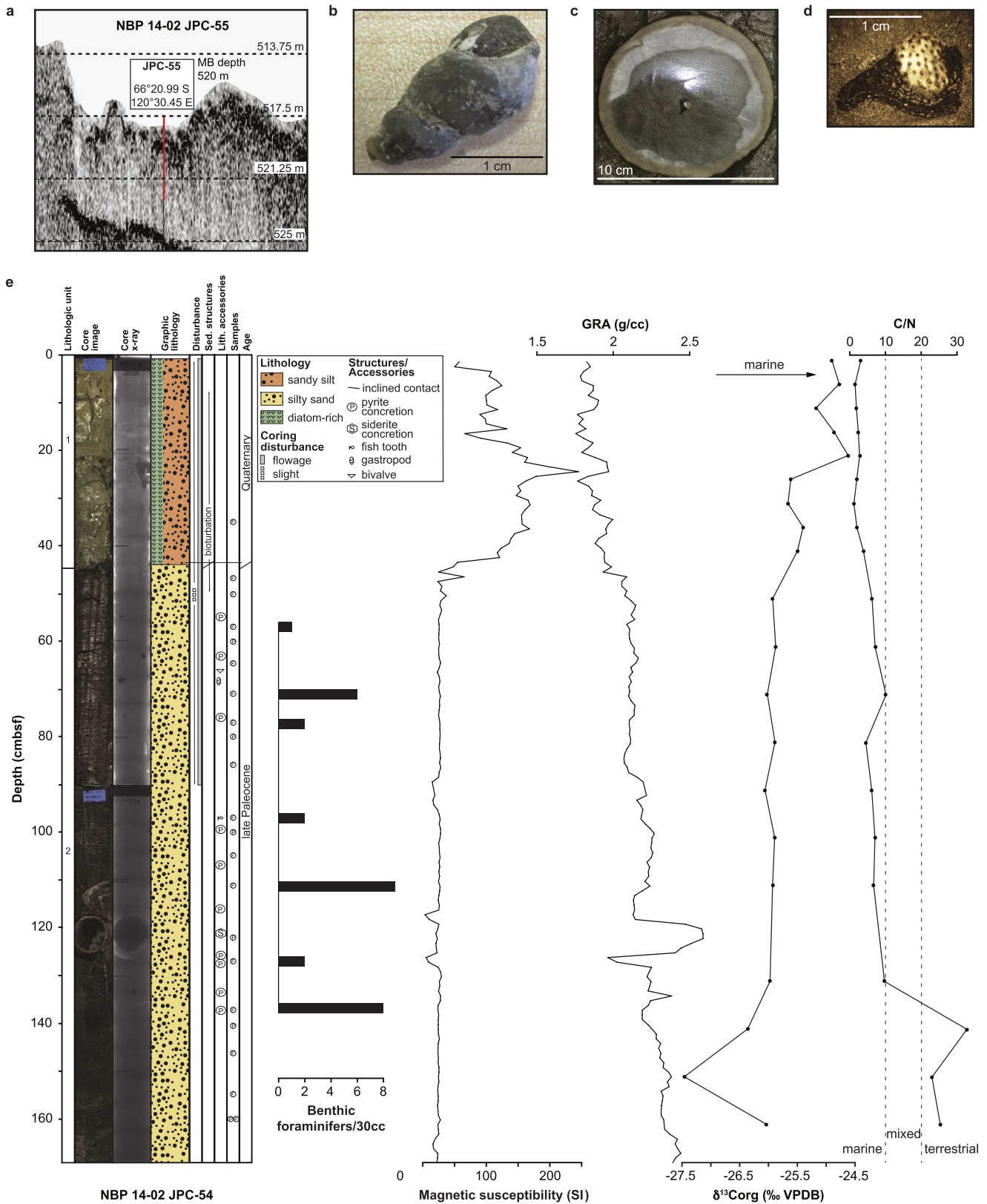
- Anderson, J. & Bartek, L. R. in *The Antarctic Palaeoenvironment: A Perspective on Global Change* (eds Kennett, J. P. & Warnke, D. A.) *Antarctic Research Series* Vol. 56, 213–263 (American Geophysical Union, 1992).
- Ó Cofaigh, C. Tunnel valley genesis. *Prog. Phys. Geogr.* **20**, 1–19 (1996).
- Huuse, M. & Lykke-Andersen, H. Over-deepened Quaternary valleys in the eastern Danish North Sea: morphology and origin. *Quat. Sci. Rev.* **19**, 1233–1253 (2000).
- Denton, G. H. & Sugden, D. E. Meltwater features that suggest Miocene ice-sheet overriding of the Transantarctic Mountains in Victoria Land, Antarctica. *Geograf. Ann.* **A 87**, 67–85 (2005).
- Loneragan, L., Maidment, S. & Collier, J. Pleistocene subglacial tunnel valleys in the central North Sea basin: 3-D morphology and evolution. *J. Quat. Sci.* **21**, 891–903 (2006).
- Elmore, C. R., Gulick, S. P. S., Willems, B. & Powell, R. Seismic stratigraphic evidence for glacial expansion during glacial maxima in the Yakutat Bay Region, Gulf of Alaska. *Geochem. Geophys. Geosyst.* **14**, 1294–1311 (2013).
- van der Vegt, P., Janszen, A. & Moscarillo, A. Tunnel valleys: current knowledge and future perspectives. *Geol. Soc. Lond. Spec. Publ.* **368**, 75–97 (2012).
- Bjarnadóttir, L. R., Winsborrow, M. C. M. & Andreassen, K. Large subglacial meltwater features in the central Barents Sea. *Geology* **45**, 159–162 (2017).
- Piotrowski, J. A. Subglacial hydrology in north-western Germany during the last glaciation: groundwater flow, tunnel valleys and hydrologic cycles. *Quat. Sci. Rev.* **16**, 169–185 (1997).
- Bart, P. J. Were West Antarctic Ice Sheet grounding events in the Ross Sea a consequence of East Antarctic Ice Sheet expansion during the middle Miocene? *Earth Planet. Sci. Lett.* **216**, 93–107 (2003).
- Scherer, R. P. A new method for the determination of absolute abundance of diatom and other silt-sized sedimentary particles. *J. Paleolimnol.* **12**, 171–179 (1994).
- Crampton, J. S. et al. Southern Ocean phytoplankton turnover in response to stepwise Antarctic cooling over the past 15 million years. *Proc. Natl Acad. Sci. USA* **113**, 6868–6873 (2016).
- Contreras, L. et al. Southern high-latitude terrestrial climate change during the Palaeocene–Eocene derived from a marine pollen record (ODP Site 1172, East Tasman Plateau). *Clim. Past Discuss.* **10**, 291–340 (2014).

44. Partridge, A. D. Late Cretaceous-Cenozoic palynology zonations: Gippsland Basin. In *Australian Mesozoic and Cenozoic Palynology Zonations (update to the 2004 Geologic Time Scale)* (ed. Montell, E.) Geoscience Australia Record 2006/23 (2006).
45. MacPhail, M. K. & Truswell, E. M. Palynology of Site 1166, Prydz Bay, East Antarctica. *Proc. ODP Sci. Res.* **188**, 1–43 (2004).
46. Truswell, E. M. & MacPhail, M. K. Fossil forests on the edge of extinction: what does the fossil spore and pollen evidence from East Antarctica say? *Aust. Syst. Bot.* **22**, 57–106 (2009).
47. Raine, J. I., Mildenhall, D. C & Kennedy, E. M. *New Zealand Fossil Spores and Pollen: an Illustrated Catalogue* 4th edn, <http://data.gns.cri.nz/sporepollen/index.htm> (GNS Science Miscellaneous Series 4, 2011).
48. Hill, R. S. (ed.) in *History of the Australian Vegetation: Cretaceous to Recent* 233 (Cambridge Univ. Press, 1994).
49. Truswell, E. M. Recycled Cretaceous and Tertiary pollen and spores in Antarctic marine sediments: a catalogue. *Palaeontographica B* **186**, 121–174 (1983).
50. Pocknall, D. T. Late Eocene to early Miocene vegetation and climate history of New Zealand. *J. R. Soc. N. Z.* **19**, 1–18 (1989).
51. Dettmann, M. E., Pocknall, D. T., Romero, E. J. & Zamalao, M. del C. *Nothofagidites* Erdtman ex Potonie, 1960; a catalogue of species with notes on the paleogeographic distribution of *Nothofagus* Bl. (Southern Beech). *N. Z. Geol. Surv. Paleo. Bull.* **60**, 1–79 (1990).
52. Stover, L. E. & Partridge, A. D. Tertiary and Late Cretaceous spores and pollen from the Gippsland Basin, southeastern Australia. *Proc. R. Soc. Vic.* **85**, 237–286 (1973).
53. Stover, L. E. & Evans, P. R. Upper Cretaceous-Eocene spore-pollen zonation, offshore Gippsland Basin, Australia. *Geol. Soc. Aust. Spec. Pub.* **4**, 55–72 (1973).
54. Harris, W. K. Basal Tertiary microfloras from the Princetown area, Victoria, Australia. *Palaeontographica B* **115**, 75–106 (1965).
55. Couper, R. A. New Zealand Mesozoic and Cainozoic plant microfossils. *N. Z. Geol. Surv. Paleo. Bull.* **32**, 1–87 (1960).
56. Raine, J. I. Outline of a palynological zonation of Cretaceous to Paleogene terrestrial sediments in west coast region, South Island, New Zealand. *N. Z. Geol. Surv. Rep.* **109**, 1–82 (1984).
57. Greenwood, D. R., Moss, P. T., Rowett, A. I., Vadala, A. J. & Keefe, R. L. Plant communities and climate change in southeastern Australia during the early Paleogene. *Geol. Soc. Spec. Pap.* **369**, 365–380 (2003).
58. Stover, L. E. & Partridge, A. D. Eocene spore-pollen from the Werillup Formation, Western Australia. *Palynology* **6**, 69–96 (1982).
59. Thomas, E. Late Cretaceous through Neogene deep-sea benthic foraminifers (Maud Rise, Weddell Sea, Antarctica). *Proc. ODP Sci. Res.* **113**, 571–594 (1990).
60. McGowran, B. Two Paleocene foraminiferal faunas from the Wangerrip Group, Pebble Point Coastal section, Western Victoria. *Proc. R. Vict.* **79**, 9–74 (1965).
61. Brotzen, F. The Swedish Paleocene and its foraminiferal fauna. *Arsb. Sver. Geol. Unders.* **42**, 1–140 (1948).
62. Holbourn, A., Henderson, A. & MacLeod, N. *Atlas of Benthic Foraminifera* (Wiley-Blackwell, 2013).
63. Li, Q., James, N. P. & McGowran, B. Middle and late Eocene Great Australian Bight lithostratigraphy and stepwise evolution of the southern Australian continental margin. *Aust. J. Earth Sci.* **50**, 113–128 (2003).
64. Tauxe, L. *et al.* Chronostratigraphic framework for the IODP Expedition 318 cores from the Wilkesland Margin: constraints for paleoceanographic reconstruction. *Paleoceanography* **27**, PA2214 (2012).



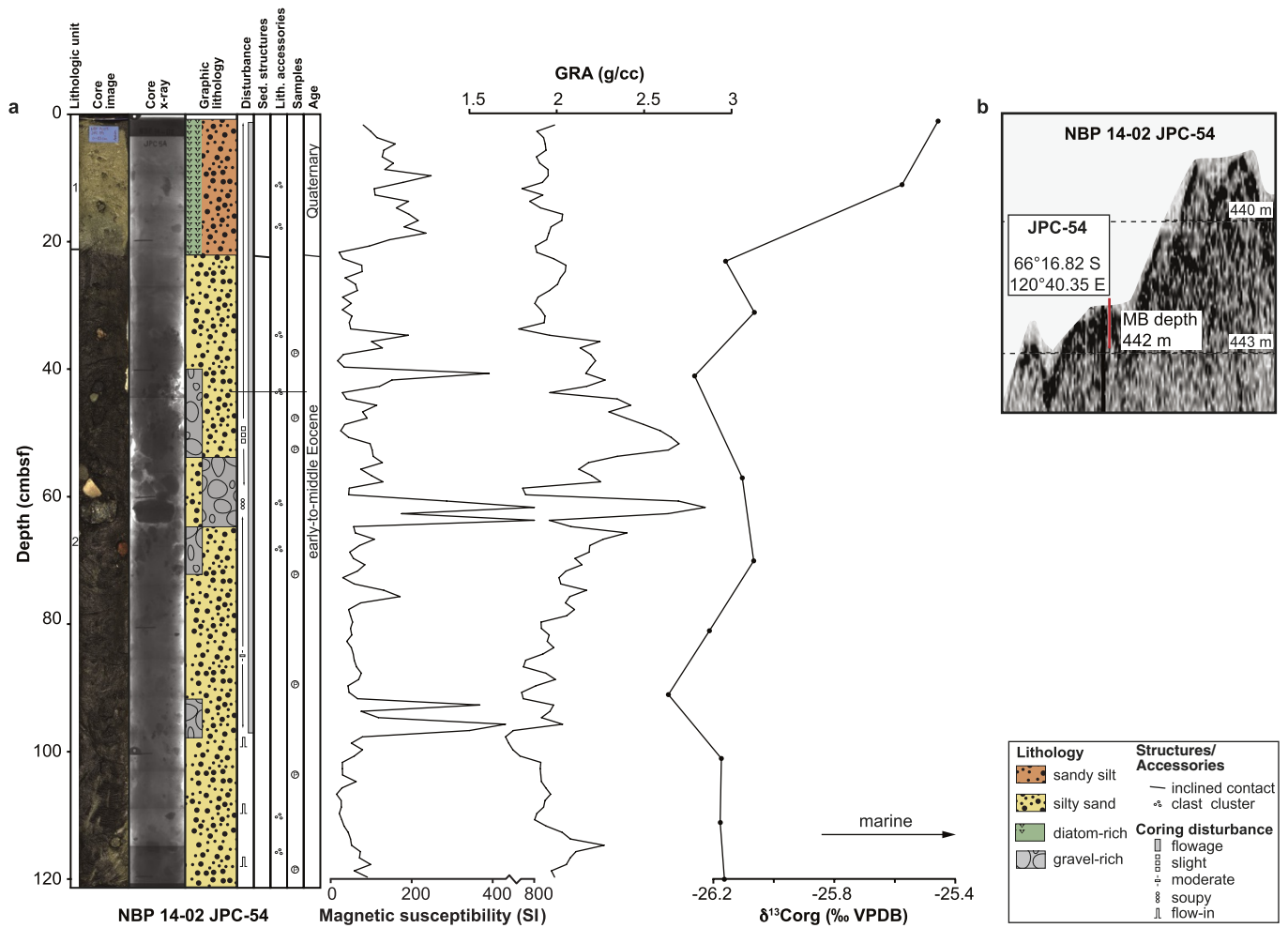
Extended Data Figure 1 | Uninterpreted NBP14-02 seismic profiles with line crossings and coring sites indicated. a, Line 13 with piston core sites JPC-30 and JPC-31 and formation penetration depths indicated by red lines. b, Line 17 with core sites JPC-55 and JPC-54 and formation

penetration depths indicated by red lines. c, Line 07 showing intersection with Line 10. d, Line 10 showing intersections with Line 07 and Line 21. e, Line 21 showing intersection with Line 10. CDP, common depth point.



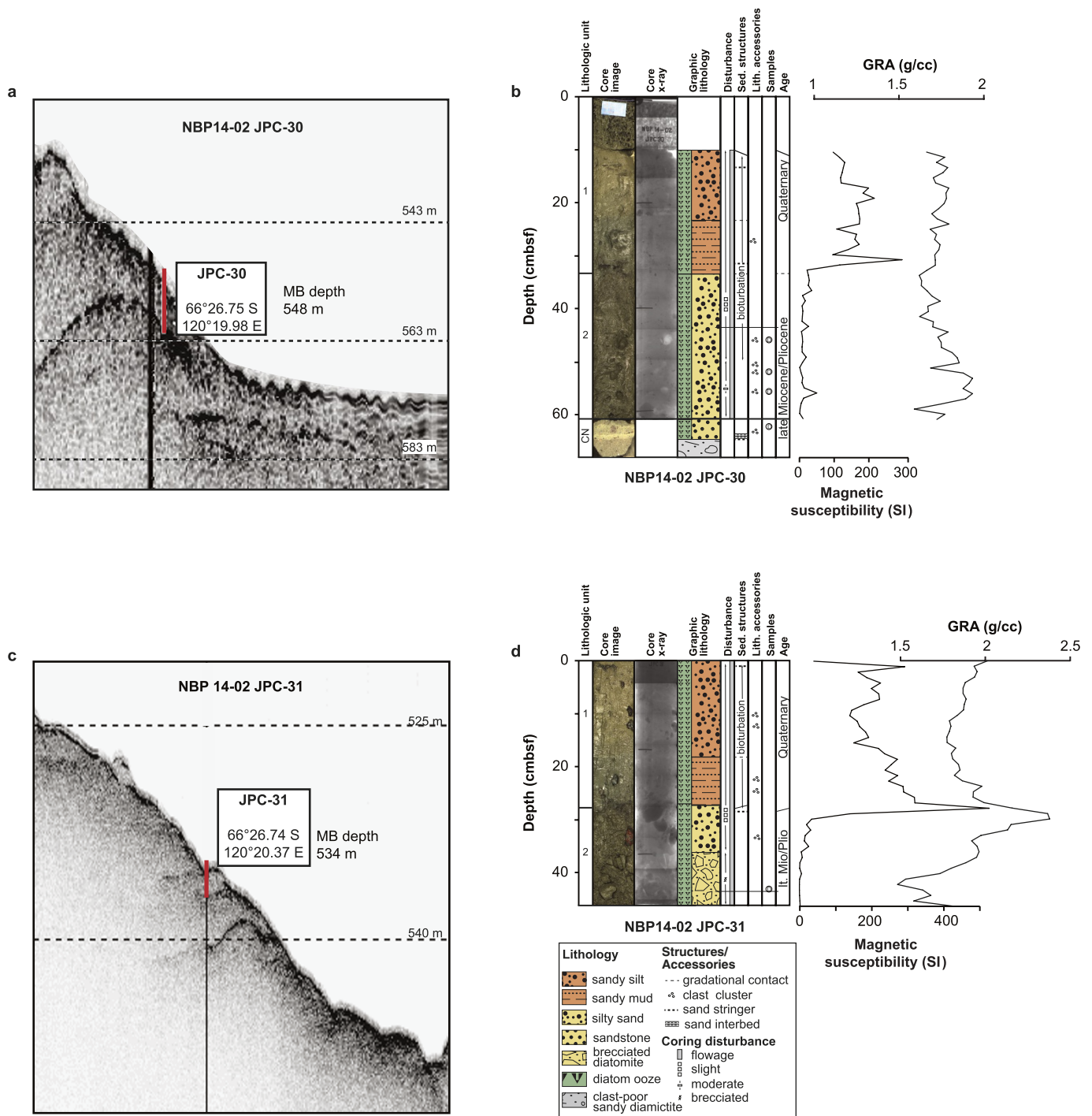
Extended Data Figure 2 | Site location and sedimentological, geochemical and palaeontological data from piston core NBP14-02 JPC-55 plotted versus depth. a, Chirp record of JPC-55 site; location and penetration indicated (red line); site coordinates and multibeam depth (MB) included. **b,** Gastropod steinkern (70–72 cm below sea floor). **c,** Siderite concretion with monocot stem nucleus (118–125 cm below sea floor). **d,** Close-up of monocot stem. **e,** JPC-55 lithologic unit, photograph,

X-ray radiograph, graphic lithology, coring disturbance, sedimentary structures, lithologic accessories (such as fossils and diagenetic features), sample locations, age, benthic foraminifers per 30 cm³ sediment, magnetic susceptibility (in SI units), gamma ray attenuation (GRA) bulk density (grams per cubic centimetre of sediment), bulk sediment $\delta^{13}\text{C}_{\text{org}}$ (per mil; VPDB‰), and carbon/nitrogen (C/N) plotted versus depth in centimetres below sea floor (cmbsf; Supplementary Information).



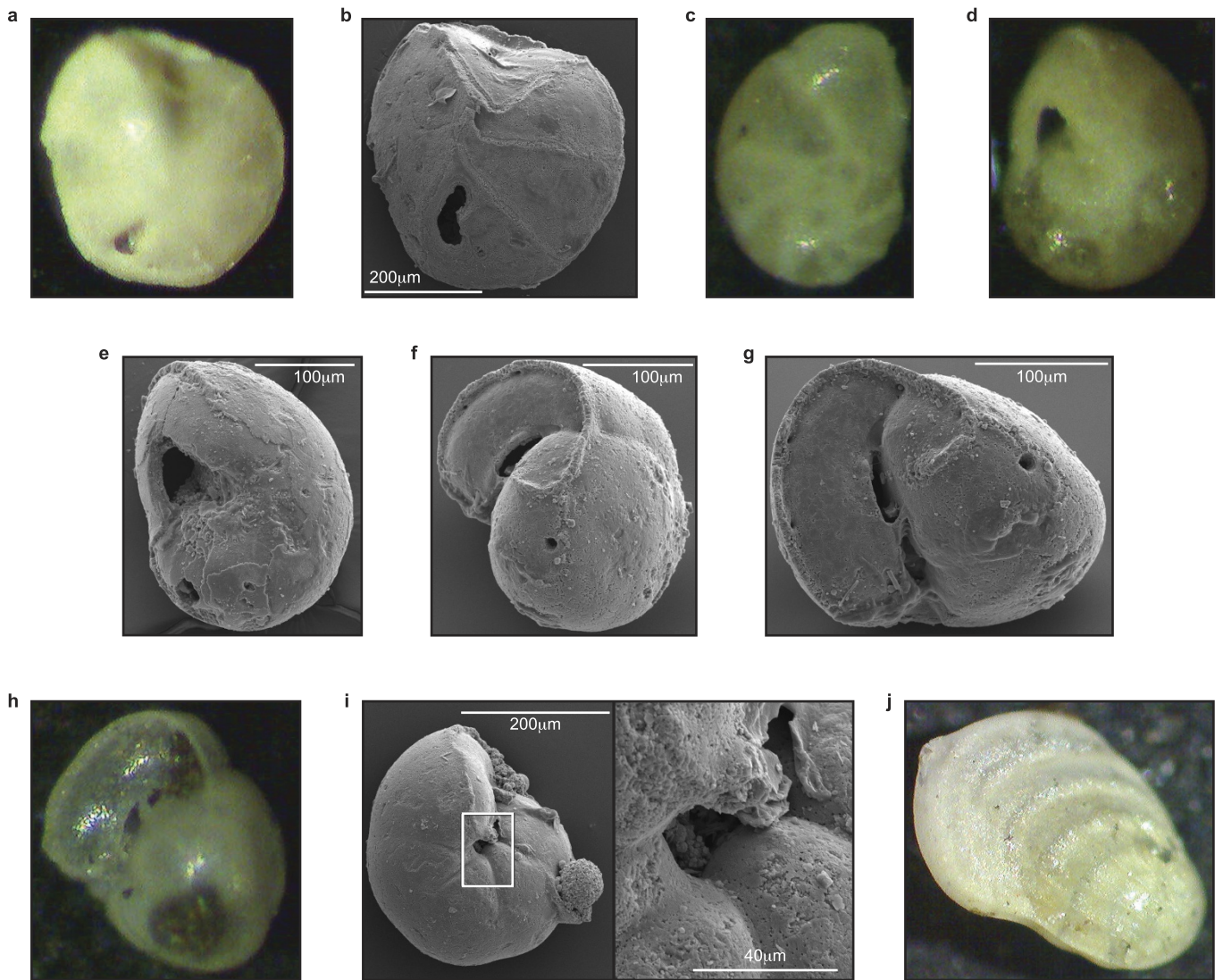
Extended Data Figure 3 | Site location and sedimentological and geochemical data from piston core NBP14-02 JPC-54 plotted versus depth. a. JPC-54 lithologic unit, photograph, X-ray radiograph, graphic lithology, coring disturbance, sedimentary structures, lithologic accessories, sample locations, age, magnetic susceptibility (in SI units;

Supplementary Information), GRA bulk density (grams per cubic centimetre of sediment), and bulk sediment $\delta^{13}C_{org}$ (per mil; VPDB‰) plotted versus depth in centimetres below sea floor (cmbsf). **b.** Chirp record of JPC-54 site; location and penetration indicated (red line); site coordinates and multibeam depth included.



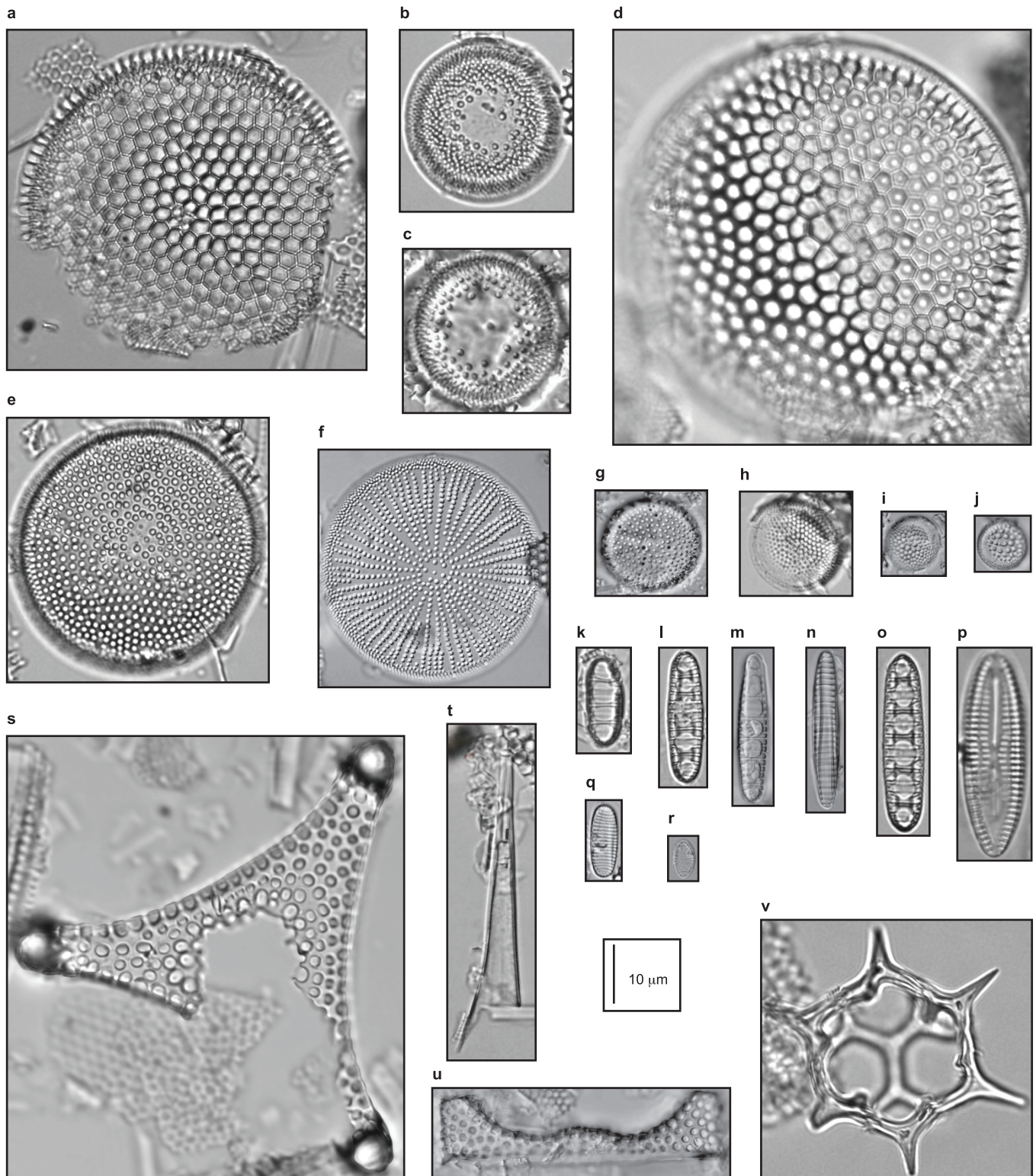
Extended Data Figure 4 | Site location and sedimentological data from piston cores NBP14-02 JPC-30 and JPC-31 plotted versus depth. **a**, Chirp record of JPC-30 site; location and penetration indicated (red line); site coordinates and multibeam depth included. **b**, JPC-30 lithological unit, photograph, X-ray radiograph, graphic lithology, coring disturbance, sedimentary structures, lithologic accessories, sample locations, age,

magnetic susceptibility (in SI units; see Supplementary Information), and GRA bulk density (grams per cubic centimetre of sediment) plotted versus depth in centimetres below sea floor (cmbsf). **c**, Chirp record of JPC-31 site; location, and penetration indicated (red line). **d**, JPC-31 lithology, age and physical properties as above.



Extended Data Figure 5 | Benthic foraminifers from piston core NBP14-02 JPC-55. **a**, *Hoeglundina elegans* (sample depth 76–78 cm below sea floor). **b**, SEM image of *Hoeglundina elegans* (76–78 cm below sea floor). **c**, *Ceratobulimina* sp. (70–72 cm below sea floor). **d**, *Ceratobulimina* sp. (70–72 cm below sea floor). **e**, SEM of *Ceratobulimina* sp. (70–72 cm below sea floor). **f**, SEM image of *Gyroidinoides globosus*

(110–113 cm below sea floor). **g**, SEM image of *Gyroidinoides globosus* (110–113 cm below sea floor). **h**, *Gyroidinoides globosus* with pyrite (136–138 cm below sea floor). **i**, *Gyroidinoides globosus* with zoom-in of umbilicus on the right; pyrite is visible on the lower right side of the test (136–138 cm below sea floor). **j**, *Palmula* sp. (136–138 cm below sea floor; test >450 μm).



Extended Data Figure 6 | Siliceous microfossils from piston core NBP14-02 JPC-31 diatomite sample. **a**, *Thalassiosira torokina*. **b**, *Thalassiosira oliverana* var. *sparsa*. **c**, *Actinocyclus ingens* var. *ovalis*. **d**, *Coscinodiscus marginatus*. **e**, *Azpeitia* sp. 1. **f**, *Actinocyclus* sp. **g**, *Actinocyclus* sp. **h**, *Shionodiscus tetraoestrupii*. **i**, *Shionodiscus tetraoestrupii*. **j**, *Shionodiscus oestrupii*. **k**, *Denticulopsis delicata*.

l, *Denticulopsis simonsenii*/*D. vulgaris*. **m**, *Denticulopsis simonsenii*/*D. vulgaris*. **n**, *Denticulopsis delicata*. **o**, *Denticulopsis simonsenii*/*D. vulgaris*. **p**, *Rouxia naviculoides*. **q**, *Fragilariopsis praecurta*. **r**, *Fragilariopsis* sp. 1. **s**, *Trinacria excavate*. **t**, *Rhizosolenia hebetate*. **u**, *Eucampia antarctica* var. *recta*. **v**, *Distephanus speculum speculum* f. *varians*. Sample taken from 43–45 cm below sea floor.

Extended Data Table 1 | NBP14-02 piston core locations, water depths, and recovered core lengths

Core ID	Latitude (°S)	Longitude (°E)	Water Depth (m)	Total length (m)
NBP14-02 JPC-30	66°26.752	120°19.984	548	0.52 plus cutter nose
NBP14-02 JPC-31	66°26.739	120°20.372	534	0.47
NBP14-02 JPC-54	66°16.815	120°40.350	442	1.21
NBP14-02 JPC-55	66°20.998	120°30.454	520	1.69

Extended Data Table 2 | Piston core NBP14-02 JPC-55 and JPC-54 raw terrestrial pollen counts

Fossil Pollen taxon*	NBP14-02 JPC-54							NBP14-02 JPC-55						
	38	46.5	53	70	91	106	120	61	81	101	123.5	141	161	
	Depth (cm)													
<i>Battenipollis sectilis</i>	23	18	4	11	10	4	15	16	7	6	8	6	14	
<i>Battenipollis</i> sp. 1 (new species)	0	5	0	0	0	1	0	70	75	49	53	65	57	
<i>Cupressacites</i> sp.	2	1	3	3	0	3	4	5	2	0	8	2	2	
<i>Cyathidites subtilis</i>	0	0	0	0	0	0	1	0	0	0	2	0	0	
<i>Dilwynnites granulatus</i> and <i>D. sp. cf. D. granulatus</i>	14	14	19	14	6	4	1	13	4	8	5	4	10	
<i>Forcipites</i> spp.	0	0	0	0	0	0	3	0	0	0	2	0	0	
<i>Gambierina edwardsii</i>	12	14	18	22	29	23	43	11	29	4	19	6	10	
<i>Gambierina rudata</i>	112	118	122	133	105	144	121	35	73	122	94	67	55	
<i>Gambierina</i> sp. 1 (new species)	0	0	0	0	0	0	0	56	35	0	0	64	43	
<i>Gambierina</i> spp.	13	8	7	0	8	6	5	2	2	17	7	4	4	
<i>Gambierina-Forcipites</i> complex (transitional forms)	3	0	1	4	6	9	0	2	3	15	15	0	1	
<i>Hexaporoicolpites</i> spp.	0	0	0	0	0	0	1	0	0	0	0	0	0	
<i>Laevigatosporites ovatus</i> & <i>L. sp. cf. L. ovatus</i>	24	10	12	26	13	10	4	14	13	15	8	8	14	
<i>Liliacidites</i> spp.	0	1	1	3	4	3	8	0	0	2	3	0	2	
<i>Microcachrydites antarcticus</i> & <i>Microalacidites paleogenicus</i>	6	0	1	0	5	0	0	1	0	0	0	0	0	
Monosulcates	7	11	5	0	0	0	0	8	3	0	0	7	6	
<i>Nothofagidites cranwelliae</i>	3	2	0	0	1	3	0	0	0	0	0	0	0	
<i>Nothofagidites emarcidus</i>	0	0	1	0	3	2	3	0	0	0	0	0	0	
<i>Nothofagidites lachlaniae</i>	0	0	0	0	0	0	0	0	1	0	1	0	0	
<i>Nothofagidites</i> sp. cf. <i>N. asperus</i>	0	0	1	1	2	0	3	0	0	2	1	0	0	
<i>Nothofagidites</i> sp. cf. <i>N. flemingii-rocaensis</i>	7	3	6	6	11	0	3	1	0	0	0	0	0	
<i>Nothofagidites</i> sp. cf. <i>N. incrassata</i>	0	0	0	0	0	3	1	0	0	0	0	0	0	
<i>Nothofagidites</i> sp. cf. <i>N. senectus</i>	0	0	0	0	0	0	0	8	7	0	0	3	4	
<i>Nothofagidites</i> spp.	12	11	14	9	14	11	10	1	4	3	10	1	0	
<i>Peninsulapollis gilli</i>	0	0	0	0	0	1	0	0	4	0	0	0	1	
<i>Phyllocladidites mawsonii</i>	0	2	2	0	0	0	4	1	1	0	0	3	2	
<i>Podocarpites</i> spp	0	2	1	3	2	0	0	0	5	0	0	0	0	
Undeterminate bisaccates	21	18	27	9	13	8	13	11	19	15	0	13	20	
<i>Podosporites-Trichotomosulcites</i> complex	0	0	3	3	3	1	0	0	0	0	0	0	0	
<i>Polypodiidites</i> sp. cf. <i>P. perverrucatus</i>	0	0	0	0	0	0	1	0	0	0	0	0	0	
<i>Proteacidites polymorphus</i>	0	1	0	2	1	3	3	0	0	0	1	0	2	
<i>Proteacidites</i> spp.	7	15	12	21	22	16	31	13	9	7	50	5	2	
<i>Proteacidites tenuixinus</i>	2	0	3	2	1	0	6	0	3	0	2	0	0	
<i>Proteacidites tenuixinus-pseudomoides</i>	0	0	0	0	0	0	4	0	0	0	0	0	0	
<i>Proteacidites-Propypollis</i>	15	13	7	8	6	7	1	13	17	20	0	17	25	
<i>Stereisporites antiquasporites</i>	1	3	0	2	0	0	1	0	0	0	3	0	0	
Tricolpate undeterminate	1	3	1	0	2	2	2	3	2	6	0	0	6	
<i>Tricolpites</i> spp.	0	2	0	0	4	1	0	0	1	3	11	5	8	
Trilete spore	5	5	6	9	7	4	5	5	3	5	0	7	1	
Various unknown	24	22	24	15	29	20	17	10	3	7	3	10	12	
TOTAL (grains per sample)	314	302	301	306	307	289	314	299	325	306	306	297	301	

*Taxa used in age determination are set in bold and italics.

Extended Data Table 3 | Piston core NBP14-02 JPC-55 raw benthic foraminifer counts

Core	Sample interval (cm)	Average depth (cm)	Sample volume (cc)	<i>Gyroidinoides globosus</i>	<i>Hoeglundina elegans</i>	<i>Ceratobulimina</i> sp.	<i>Palmula</i> sp.	Total benthic foraminifers /30cc	Benthic foraminifers	Notes
JPC-55	35-37	36	20	0	0	0	0	0	0	
JPC-55	46-48	47	30	0	0	0	0	0	0	
JPC-55	50-52	51	20	0	0	0	0	0	0	
JPC-55	56-58	57	30	1	0	0	0	1	1	
JPC-55	66-68	67	30	0	0	0	0	0	0	
JPC-55	70-72	71	20	2	1	1	0	4	6	
JPC-55	76-78	77	30	1	1	0	0	2	2	
JPC-55	86-88	87	30	2	0	0	0	2	2	
JPC-55	96-98	97	30	1	1	0	0	2	2	fish tooth
JPC-55	106-108	107	30	0	0	0	0	0	0	
JPC-55	110-112	111	20	5	0	1	0	6	9	
JPC-55	126-128	127	30	2	0	0	0	2	2	
JPC-55	136-138	137	30	7	0	0	1	8	8	
JPC-55	146-148	147	30	0	0	0	0	0	0	
JPC-55	156-158	157	30	0	0	0	0	0	0	
JPC-55	161-163	162	20	0	0	0	0	0	0	